Demonstration of a remotely piloted atmospheric measurement and charge release platform for geoengineering

Article

Accepted Version

Harrison, G. ORCID: https://orcid.org/0000-0003-0693-347X, Nicoll, K. ORCID: https://orcid.org/0000-0001-5580-6325, Tilley, D. J., Marlton, G., Chindea, S., Dingley, G. P., Iravani, P., Cleaver, D. J., duBois, J. L. and Brus, D. (2021) Demonstration of a remotely piloted atmospheric measurement and charge release platform for geoengineering. Journal of Atmospheric and Oceanic Technology, 38 (1). pp. 63-75. ISSN 1520-0426 doi: 10.1175/JTECH-D-20-0092.1 Available at https://centaur.reading.ac.uk/93830/

To link to this article DOI: http://dx.doi.org/10.1175/JTECH-D-20-0092.1

Publisher: American Meteorological Society

Demonstration of a remotely piloted atmospheric measurement and charge release platform for geoengineering

R. Giles Harrison[1*], Keri A. Nicoll[1,2], Douglas J. Tilley[2], Graeme J. Marlton[1], Stefan Chindea[2], Gavin P. Dingley[2], Pejman Iravani[3], David J. Cleaver[3], Jonathan L. du Bois[3], David Brus[4]

accepted by *Journal of Atmospheric and Oceanic Technology* 4th November 2020

[1] Department of Meteorology, University of Reading, Reading, RG6 6BB, UK

[2] Department of Electronic and Electrical Engineering, University of Bath, Bath, BA2 7AY, UK

[3] Department of Mechanical Engineering, University of Bath, Bath, BA2 7AY, UK

[4] Finnish Meteorological Institute, PO Box 503, FI-00101, Helsinki, Finland

*corresponding author: r.g.harrison@reading.ac.uk

Abstract

Electric charge is always present in the lower atmosphere. If droplets or aerosols become charged, their behaviour changes, influencing collision, evaporation and deposition. Artificial charge release is an unexplored potential geoengineering technique for modifying fogs, clouds and rainfall. Central to evaluating these processes experimentally in the atmosphere is establishing an effective method for charge delivery. A small charge-delivering Remotely Piloted Aircraft has been specially developed for this, which is electrically propelled. It carries controllable bipolar charge emitters (nominal emission current ±5 μA) beneath each wing, with optical cloud and meteorological sensors integrated into the airframe. Meteorological and droplet measurements are demonstrated to 2 km altitude by comparison with a radiosonde, including within cloud, and successful charge emission aloft verified by using programmed flight paths above an upwards-facing surface electric field mill. This technological approach is readily scalable to provide non-polluting fleets of charge-releasing aircraft, identifying and targeting droplet regions with their own sensors. Beyond geoengineering, agricultural and biological aerosol applications, safe ionic propulsion of future electric aircraft also requires detailed investigation of charge effects on natural atmospheric droplet systems.

Keywords: aerosol charging; corona emission; meteorology; cloud; Unmanned Aerial Vehicle (UAV); Unmanned Aircraft System (UAS);

1. Introduction

Electricity in the atmosphere has long been supposed to influence clouds of water droplets. For example, Luke Howard (1772-1864), whose cloud nomenclature system is still widely used, stated that in nimbus (rain) clouds, water drops *“...are by a change in their electrical state made to coalesce, and descend in drops of Rain.”* (Howard, 1837). This assertion probably arose from the then fashionable interest in electrostatics rather than observations, but Lord Rayleigh (Rayleigh, 1879) subsequently reported direct experiments in which *“Instead of rebounding after collision, as the unelectrified drops of water generally or always do, the electrified drops coalesce…”*. More recent experimental and theoretical work (e.g. summarised in Pruppacher and Klett, 1998) has confirmed that charge does indeed influence droplet collisions and coalescence, and empirical findings indicate that regional ionisation release is associated with precipitation changes (Harrison et al, 2020). Highly charged droplets are also known to disintegrate under intense electric forces (Rayleigh, 1882; Duft et al, 2003). Here we demonstrate a new enabling technology to modify droplet electrostatics as a potential geoengineering technique, through releasing charge from a remotely controlled platform capable of entering clouds or aerosol regions. We describe a Remotely Piloted Aircraft (also known as an Unmanned Aircraft System, UAS) from which ions of either polarity can be released in a regularised manner, also providing an on-board measuring capability with which the local droplet, thermodynamic and electrical conditions can be monitored.

A great advantage of charge release as a possible geoengineering approach using airborne platforms is that large volumes of modifying substance are not required to be carried aloft. It is consequently well suited to the capabilities of small Remotely

Piloted Aircraft (RPA), equipped with charge emitters and monitoring instrumentation, as summarised in figure 1. The technology developed is described here. Section 2 assesses the requirements for an ion release system from which generated ions ultimately become attached to water droplets, charging them. Section 3 describes the charge emission and meteorological sensing technology developed and Section 4 the integration of this technology with an aircraft. Addressing the practical difficulties of flying beyond visual line of sight into clouds is a further essential aspect, to obtain good operating duration (tens of minutes) at significant altitude (to several km). Section 5 describes trials of the system in specially arranged airspace and section 6 evaluates the charge emission.

For such a widespread and fundamental influence as electrostatics on droplet behaviour there are many other associated applications, including in biology, for which droplet charging is recognised to enhance insect and foliage deposition (Gaunt et al 2003; Inculet et al, 1981). Investigating the effect of charge on the efficiency of airborne aerosol sampling provides a further application. Beyond aerosol physics, biological systems and geoengineering, additional motivation is provided by the need to explore atmospheric consequences of future electric propulsion of aircraft by ion emission (Xu et al, 2018; Ieta and Chirita, 2020). The net electrostatic effects within natural aerosol systems, and their influence on detailed microphysical droplet processes leading to rain, remain to be explicitly quantified, for which the new experimental capabilities described are highly suitable.

2. Charge release considerations

Charging of water droplets can be achieved by release of air ions into the droplet region (e.g. Gunn, 1954). The charge modifies the behaviour of the droplets, especially that concerned with droplet-droplet collisions. This is now discussed further, together with estimates of the charge required and generated.

(a) Properties of charged droplets

When a charged water droplet approaches another water droplet, charged or uncharged, it induces a charge in the second droplet, which induces a further charge in the original droplet, repeating indefinitely. Charged, colliding water droplets therefore experience an infinite system of electrostatic image charges between them, with associated electric forces (Thomson,1853; Russell, 1922; Davis, 1964). Formally, the net droplet-droplet force is always attractive at small separations regardless of the droplets' relative polarities, unless the exact ratios of their charges would make them an equipotential on contact (Lekner, 2012; Banerjee and Levy, 2015). With natural variability, this unique equipotential condition is unlikely to occur, hence two colliding charged cloud droplets can be generally considered as being more likely to coalesce than two neutral droplets. Therefore, if cloud droplets can be charged artificially, the electrical influence on coalescence may, in turn, hasten the generation of rain (Harrison et al, 2015). Another application for artificial charge dispersal might arise from the practical need to remove droplet or aerosol charge, such as in the case of release of radioactive aerosol, which can become sufficiently highly charged to be preferentially washed to the surface by water droplets (Tripathi and Harrison, 2001).

Release of corona ions into fogs and clouds has been contemplated previously and considered for possible hydrological and electrical benefits. After observing a fog near a high voltage tower, the inventor and electrical engineer, Nikola Tesla (1856-1943), said *“I am positive…that we can draw unlimited amounts of water for irrigation”* (Cheney, 2001). The most well-known artificial charge release work is probably that of Vonnegut and Moore, in which corona ions were released from near-surface high voltage horizontal wires 14 km long (Vonnegut et al 1962a,b). With this apparatus, it was demonstrated that the charge released modified the initial electrification of small cumulus clouds. Later work (Phelps and Vonnegut ,1970), estimated the charging needed to influence the droplet growth.

(b) Requirements for charge release

Introducing charge into an aerosol or cloud can be achieved through surface or airborne release of air ions. Surface emission systems require extensive installations, and depend on natural updrafts and entrainment processes to allow the generated ions to reach and enter aerosols or clouds. As substantial quantities of ions can be generated relatively easily, the inefficiency of the vertical transport process may not matter in allowing some additional ions to ultimately reach and enter clouds, through following natural updraft routes. The disadvantage is that, even with large quantities of charge generation at the surface, assessment of any consequent effects will be complicated by the wide spatial dispersion of ions likely to be encountered. Using aircraft to provide targeted charge release controlled from the surface provides a promising alternative, allowing cloud regions to be located where small droplets, which are those most likely to be influenced electrically, are more abundant. In addition, because charge can be generated easily electrically, there are no substantial payload requirements and hence small aircraft are particularly suitable.

Although more detailed work at local scales is needed to fully evaluate the charge required to influence natural aerosols and clouds, some bounding estimates can be made. The regional scale cloud and precipitation changes reported by Harrison et al (2020) were associated with an approximate doubling of the natural ion concentration. Over land surfaces, the typical volumetric ion production rate q_0, is about 10^7 ion pairs m^{-3} s^{-1} (Chalmers, 1967). This reduces with height, before increasing from cosmic ray ionisation above about 3 km. If clear air is considered (i.e. neglecting ion removal to aerosol or droplets), the steady-state mean ion number concentration n_0 is given by

$$n_0 = \sqrt{\frac{q_0}{\alpha}} \qquad (1)$$

where α is the ion-ion recombination rate (1.6×10^{-12} m^3 s^{-1}). For $q_0 = 10^7$ m^{-3} s^{-1}, this gives n_0 = 2500×10^6 m^{-3} (Harrison and Carslaw, 2003).

For an air ion generator operating by corona emission, the associated unipolar ion production rate, neglecting recombination, is directly proportional to the current flowing to the emitter tip. If the corona current is I_c, the corona ion production rate R_c will be

$$R_c = \frac{I_c}{e} \qquad (2),$$

where e is the elementary charge (1.6×10^{-19} C). If the aircraft is in level flight at a speed v, and air ions are emitted in a cylindrical beam of cross section area S, the instantaneous number of unipolar ions, n_c, generated per unit volume due to corona is

$$n_c = \frac{R_c}{Sv} = \frac{I_c}{Sve} \quad (3).$$

The current required to generate an instantaneous corona ion concentration which is a multiple f of the steady-state background ion concentration n_0 (i.e. $f = n_c/n_0$), is therefore

$$I_c = fSve\sqrt{\frac{q_0}{\alpha}} \quad (4).$$

For a small aircraft (1 m wingspan) flying at v = 30 ms^{-1}, emitting an ion plume into an area defined by the wingspan (i.e. S =1 m^2), I_c is found from eqn (4) for f =1 as ~10^{-8} A. If, as observing smoke plume releases from small aircraft suggests, the emitted ion plume spreads vertically by up an order of magnitude more, S ~100 m^2 and the associated I_c required is ~10^{-6} A. Emission currents of at least 10^{-6} A (i.e. 1μA) are realisable, hence f >>1 from a practical emission system is readily obtained. The total cloud volume into which ions are released is determined by the flight path and duration.

An alternative perspective was provided by Phelps and Vonnegut (1970), who estimated that, to increase the coalescence efficiency of droplets to near 100%, an oppositely charged droplet carrying an order of magnitude more charge than the surrounding droplets would be needed. Takahashi (1973) showed that the average charge on a droplet in a warm cloud was approximately 1×10^{-17} C (~60$|e|$) Thus, for enhanced coalescence, a charge of 1×10^{-16} C would be needed on half of the cloud droplets. Assuming a cloud droplet concentration of 100 cm^{-3} this would require a charge delivery rate of 10 nC m^{-3}. With the typical RPA air speed assumed of v = 30 ms^{-1}, a charge delivery system would therefore need to provide 0.3 μA m^{-2} which is similar to that estimated above.

Releasing unipolar charge will also affect the electric potential of the aircraft compared with the local environmental potential, as the aircraft will develop an opposite charge equal in magnitude to the charge released. The charging rate of the aircraft can be estimated as

$$\frac{dV}{dt} = \frac{I_c}{C} \quad (5),$$

where $\frac{dV}{dt}$ is the rate of change of the potential of the aircraft and C is the aircraft's capacitance. If the aircraft is considered as an isolated spherical capacitor of radius 1 m, C ~100 pF, and the associated $\frac{dV}{dt}$ for I_c = 10 nA will be 90 V s^{-1}. This is likely to overestimate the charging rate, as any loss of charge from the aircraft is neglected. This could occur by collision or attraction of atmospheric space charge, which would act to reduce the charging rate.

The limitations on unipolar charge release implied by eqn (5) are important, as if the charge emission continues indefinitely, the electric field at the surface of the aircraft will ultimately become dangerously large, leading to systems failure through electrostatic discharge damage, and possible loss of the aircraft. (In the case of ion thrusters for spacecraft, neutralisers are specifically included to avoid this e.g. Kent et al, (2005)). This risk can be reduced by approximately balanced emission of positive and negative charge, as then the aircraft charging will be less rapid, determined by the difference in the emission currents which is likely to be smaller than their absolute magnitude. A discharge wick, widely used on traditional aircraft, provides another possibility. A consequence of bipolar emission is, however, that the loss of corona ions by recombination will be increased.

A controllable RPA charge emission system developed is now described (section 3) able to provide up to ± 5 μA of corona current, followed by considerations associated with its integration into the aircraft (section 4). Flight tests evaluating the meteorological and electrical aspects are described in section 5.

3. Aircraft charge emitters

The charge emitters emit corona ions from a carbon fibre brush, raised to a high voltage. Two separate unipolar emitters are used, controllable to release positive and negative charge independently. These were designed to have a physical form (130 mm x 40 mm x 40 mm) and mass (100 g) suitable for small aircraft, and to operate from a 12 V power supply. Each emitter's current varies with the operating voltage chosen, which is remotely controllable through the aircraft telemetry (figure 2). The currents supplied to the emitting tips can be monitored, which allows the positive and negative currents to be balanced, to minimise the aircraft charging hazard. Because the current measurement has to be obtained at the emission (high voltage) part of the corona emitter circuit, an isolated system is required to provide the measurement at safe voltages for the aircraft's data telemetry. Communication between the aircraft system and the emitters is therefore required in two directions, from the aircraft to the emitter to set the high tension operating voltage (which is also confirmed back), and from the emitter to the aircraft to report the corona current. This information is recorded by the aircraft data system.

In each charge emitter, the operating high voltage is requested by the aircraft's data logger, over a USB-UART serial link, and the resulting output current monitored. Within each emitter, a microcontroller acts as the main control and communication link between the aircraft and the device, providing control of the high-voltage module and monitoring of the output voltage, while another internal UART serial link communicates over an optical isolator with the current sensing section.

The amount of ion production is determined by the current flowing from the high-voltage module through the discharge brush into the surrounding environment. This current is monitored by measuring the voltage drop across a series resistor, between the module output and emitting tip. Since the current sense circuit is elevated to the potential of the high-voltage output of the module, the measurements are returned through an optical link (e.g. Harrison 2002; Aplin et al 2008), with its supply galvanically isolated from the low voltage section of the board. A chain of three transformers (type PT6) with their secondaries in series is used to provide a total isolation of 9 kV, using a square wave oscillator drive, as shown in Harrison (1997).

The actual output currents from the charge emitters were characterised using the experimental arrangement summarised in Figure 3. For this, the emitting tip (a carbon fibre discharge brush) of the charge emitter was mounted on a PTFE stand-off, within a large grounded diecast box. The discharge tip was pointed at a brass detector plate connected to a trans-resistance converter (using a 1 MΩ feedback resistance) circuit, to measure the corona ion current flowing to the brass plate at the local ground potential. The detector plate was mounted centrally within the box, to allow operation of the two emitters either side of the detector plate symmetrically. Through this arrangement, balancing of the output currents from both emitters was achieved by independently adjusting their operating high tension (HT) voltages, until the opposite currents were sufficiently similar that no net plate current was measured.

Figure 4(a) shows the current measured by the detection plate as the operating voltage of the corona emitters was varied. The onset threshold for corona emission is also related to the precise emitter tip shape, but was found to be around 1200 V for the negative emitter and 2300 V for the positive emitter. The absolute current measured by the detector plate depended on the geometry, as varying the distance between the discharge wick and the plate changed the effectiveness of ion capture and the associated detector plate current. Figure 4(b) shows the operation of the onboard isolated corona current measurement circuit when the corona current was varied, by changing the HT voltage. The linear relationship found between the corona current and HT voltage demonstrates that, through adjusting the HT voltage, the emission current can be altered in flight.

4. Aircraft science equipment integration

The RPA platform chosen for this work is the commercially available Skywalker X8 fixed wing aircraft. Use of a standard platform allows for possible scaling up to a fleet of aircraft. The X8 is capable of the long-range operations required to fly into clouds, including an ability to climb to altitudes of 3 km. It is a flying wing design made of expanded polyolefin foam, with a single folding propeller in a pusher configuration. It has a wingspan of 2.1 m and maximum take-off mass of 5 kg, with capacity to carry scientific equipment in a small payload bay at the front of the aircraft. The “pusher” configuration allows the science instrumentation to be located far from the propellers and noise generating components, reducing electrical interference on the measurements. In use, the RPA is flown autonomously using a Pixhawk 2.1 Cube autopilot with Arduplane software (V3.9.6), propelled by a Cobra 3520 550Kv motor with Aeronaut 13” x 8 propellors and a FrSky Neuron 60 Electronic Speed Controller. UHF control links are made at 868 MHz. Separate 3000 mA h and 4000 mA h LiPo batteries are used to power the systems and propulsion motor respectively.

The locations of the various science sensors installed on the aircraft are shown in Figure 5. As the RPA is designed to fly within, and sample, cloud properties, it has been instrumented with temperature (RSPRO 2.4mm diameter bead thermistor) and RH sensors (Honeywell HIH-4000), and an optical cloud sensor (OCS) (Harrison and Nicoll, 2014) located in the front of the aircraft, pointing downwards to minimise water ingress and to provide shielding from solar radiation. Atmospheric space charge density sensors (with both linear (Nicoll, 2013) and logarithmic (Harrison et al, 2017) responses) are also located in the front of each wing to monitor the charge environment surrounding the aircraft. Data from all the science sensors are logged at 1 Hz through a custom-made data logging board based on a TinyDuino (an ATMEGA328-based device) as the main processor, carrying its own GPS and data storage.

Mounting positions for the corona emitters are also shown in Figure 4, on the underside of the wings, approximately 20 cm from the propellor, facing backwards. The positive corona emitter is located on the left wing, the negative emitter on the right wing. This positioning ensures that the corona ions are emitted into the turbulent flow behind the aircraft, helping to disperse the ions and ensuring they do not return to the aircraft, which would modify its charge. The corona emitters can be switched independently to provide positive, negative or bipolar ion emission, using optically isolated switches activated by the pilot through the remote control (RC).

5. Flight tests of aircraft instrumentation

Separate series of flight tests were undertaken to evaluate the flight endurance and payload capability, meteorological measurements and charge emission. Calibration information on the sensors is provided in the Appendices.

(a) Aircraft aspects

To examine the flight capabilities of the extensively instrumented Skywalker airframe, test flights were conducted at the Pallas Atmosphere-Ecosystem Supersite, in sub-Arctic Finland during the Pallas Cloud Experiment (PaCE 2019) (Latitude 68.01˚N, Longitude 24.14˚E) during September 2019. This site had a designated Temporary Dangerous Area (EFD527), permitting flights to a ceiling of 2 km Above Mean Sea Level (AMSL). Table 1 summarises all the RPA flights undertaken, including details of the eleven flights conducted at Pallas. The longest endurance flight path is shown in figure 6.

The maximum altitude reached in this flight was 2000 m AMSL in a flight duration of 20 min 45 s. This consisted of a 11 min climb at a 10° angle to 2000 m, followed by a 9 min glide to landing. The principal battery usage occurred during the climb, requiring a mean current of 16 A compared with 0.2 A during the descent. Over the entire flight, the total charge drawn from the propulsion battery was 3850 mA h, of the 4000 mA h nominally available.

(b) Meteorological sensors

The meteorological measurements made by the X8 RPA during flight were compared with nearby meteorological measurements made using a balloon-carried instrument package, employing an RS41 radiosonde augmented with additional science sensors.

The balloon payload consisted of a standard Vaisala RS41 radiosonde with an optical cloud sensor (OCS) (Harrison and Nicoll, 2014) and charge sensor (Nicoll, 2013) attached, of identical design to those on the aircraft. The add-on sensors were housed in a 3D printed enclosure. This enclosure had fixing spikes printed to grip into the RS41's polystyrene shell, firmly securing the add-on sensors with a tensioned cable tie. Data from the sensors was relayed through the RS41's telemetry system using the ozone sensor (OIF411) port, following Harrison et al (2012). The sensor data was interleaved with the RS41's data-stream and recorded by the ground station. The additional data packets were synchronised with the standard meteorological data after the ascent. The RS41 carried standard temperature and humidity sensors, having a quoted accuracy of ±0.01 ˚C and ± 0.1 % respectively (Vaisala 2018):

An Intense Observation Period was undertaken at the Pallas site on 27th September 2019 to compare the balloon and aircraft systems. For this, a fully instrumented RPA flight into a thin stratiform cloud was made, followed by a RS41-special sensor balloon launch to provide reference data. The radiosonde and aircraft data obtained are now compared.

Figure 7a and b show the standard thermodynamic meteorological quantities from the RS41 radiosonde in black, and the X8 aircraft in red. From the temperature and RH data a cloud layer 100m thick at approximately 1700m is apparent. The cloud top is capped with a 5 ˚C inversion at 1800m. Figure 7a demonstrates a -2 ˚C cold bias of the temperature sensor on the X8 when compared to the RS41 temperature sensor, which can be corrected in future flights. The X8's RH sensor tracked the RS41 sensor closely, except in the cloud top region at 1800 m where it lagged the RS41, taking longer to adjust to the cloud features. As the radiosonde and the X8 each encountered the cloud layer at different speeds, displaced in time, their lag times cannot be uniquely identified. The response time of the RS41's humidity sensor is given by the manufacturer (Vaisala, 2018) as less than 0.3s at 20˚C and less than 10s at -40˚C.

Figure 7c shows the charge density from the port wing-mounted charge sensor, plotted alongside the charge density inferred from the charge sensor data from the radiosonde. The charge was calculated following Nicoll and Harrison (2016). In the cloud at 1700 m the wing mounted charge sensor detected a maximum positive charge density of approximately 50 pC m^{-3}; the radiosonde detected a similar maximum positive charge density of 60 pC m^{-3}. Such extensive layer clouds often show charging associated with the upper and lower cloud boundaries (Nicoll and Harrison, 2016). The two traces demonstrate similar charge profiles from two different measurement platforms which encountered the same cloud environment.

The greater variability apparent in the X8 profiles may be due to additional electrical noise from the aircraft systems, or naturally generated lateral charge variations.

Finally, cloud droplet number concentrations derived from the OCS on the two measurement platforms are compared in Figure 7d. Both OCSs on the radiosonde and X8 aircraft recorded peak droplet concentrations of 150 cm^{-3} within the cloud layer. (The method of calculation of the droplet concentration from the raw sensor output is described in Supplementary Information S1).

In summary, the instrumented X8 airframe can provide thermodynamic, electrical and optical measurements in cloud, at up to 2000 m above the surface.

(c) Charge emission aspects

Further trials were undertaken to test the operation of the corona emitters in flight and quantify the emitted charge during ow level flying over a surface electric field instrument. Positive charge emission from the aircraft would result in a positive electric field perturbation beneath and a negative field perturbation for negative charge emission. Flights were performed at the University of Bristol's Fenwood Farm, Long Ashton, UK (51.423˚N, -2.671˚W). The site is a large flat agricultural pasture without obstacles. Two flights were conducted on the 29th November 2019, under fair weather conditions with clear skies and no appreciable local charge generation from meteorological processes. (Details of these further flights are also provided in Table 1). Detection of the aircraft's charge emission was made using a Chubb JCI131 electric field mill (EFM), to measure the vertical electric field at the surface. The EFM was mounted on a 3m high vertical mast, separately calibrated to correct for the electric field distortion due to the presence of the earthed mast. The measurement range of the EFM was ±2 kV m^{-1} with a resolution of 0.1 V m^{-1}, and values logged at 1 Hz.

To detect charge emission from the aircraft, a stable and reliable pattern of corona emission was required, which was achieved through conducting flight operations automatically to maintain consistent flight paths. Each mission was divided into three separate operational stages. Initially, a rectangular flight path conducted at 50 m altitude was used to ensure that the aircraft was operating correctly. This was followed by level flight operations above the EFM. Finally, a circular, unlimited loiter pattern was made above the EFM. The mean loiter speed of the aircraft was 19 m s^{-1} and the total flight time was 17 mins.

Figure 8a shows details of the flight path, demonstrating the level flight operation legs, and the indefinite circular loiter pattern. The circular loiters were conducted at 15 m and 20 m above ground level, with a 50 m radius. Each loiter was planned to position the edge of the flying circle above the EFM.

Figure 9 shows the surface electric field, E, time series during the X8's second flight. Markers show when either corona emitter was switched on and off. Whenever one emitter was activated on the aircraft, a transient change in E was detected beneath. For positive corona, E increased and for negative corona events E decreased. When, however, both emitters were activated there was a negligible change in E, which indicates that the opposite polarities act to cancel the point charge, as perceived by the EFM.

The densest region of charge emitted by the aircraft can be considered quantitatively to be represented by an equivalent point charge above the EFM. For a point charge Q, the electric field E induced by the point charge at distance r is given by

$$E = \frac{Q}{4\pi\varepsilon_0 r^2} \quad (6),$$

where ε_0 is the permittivity of free space and r becomes the height of the aircraft above the EFM. By using a smoothing spline (with a unit smoothing parameter for a piecewise cubic spline interpolation), to detrend the electric field time series to retain only the transient changes (as shown in figure 10), the emitted charge from the aircraft can be calculated from eqn (6). Using this methodology, the mean of the inferred point charges for the five positive and five negative transients observed in Figure 10 was found to be 0.43 μC when the positive emitter was activated, and -0.35 μC when the negative emitter was activated. The small magnitude difference is likely to be associated with the different magnitudes of operating currents from the two emitters (calculated to be 5.3 μA and -2.8 μA for the positive and negative emitters respectively). The detected charge was evidently much less (90%) than the instantaneous charge emitted. For an emitter current of ~5 μA, a charge of ~5 μC would be expected to be observed when the RPA passed directly over the electric field mill. These measurements, when combined with the findings in figures 3 and 4, indicate that most of the released ionic charge is rapidly dispersed in the atmosphere, to be removed through ion recombination or attachment to boundary layer aerosol (Harrison and Carslaw, 2003). The charge removal to droplets in a cloud situation can be expected to be similar, with the mixing processes associated with the turbulent air behind the aircraft acting to spread the air ions released.

(d) Summary

Taken together, the evaluations undertaken in sections 5a, b and c show that the objectives stated in the opening paragraph have been addressed and specifically that the instrumented aircraft is able to:

(1) carry scientific payload to cloud-level altitudes, with an endurance of ten minutes

(2) provide thermodynamic meteorological profile information

(3) locate cloud regions through the combination of a rapid time response relative humidity sensor and an optical cloud sensor using backscattered light from the water droplets

(4) deliver charge in a controllable and monitored manner, of either, or both polarities.

Further, the commercial airframe employed and the standard devices and components used in construction of the instrumentation make the production of multiple aircraft readily achievable, to increase the volume of cloud which can be intermittently sampled or continuously interacted with.

6. Conclusions

The instrumented RPA platform described here generates a new capability for cloud and aerosol investigations, and for assessing effects on their electrical behaviour following charge release. It successfully provided thermodynamic, optical and electrical properties of clouds at heights up to 2 km, allowing most boundary layer clouds to be accessed and studied, as well as mists, fogs and aerosol plumes. The novel combination of a controllable bipolar charge delivery system with integrated optical sensors allows cloudy regions to be identified and targeted remotely or autonomously. Future use of electric aircraft by ionic propulsion, or the neutralisation of highly charged particle clouds presenting electrostatic hazards, illustrate further environmental applications which may benefit from targeted charge release capability.

Atmospheric charge release has established biological and agricultural applications and may ultimately have a new use in geoengineering through providing cloud droplet charging. This work shows that charge delivery into large atmospheric volumes can be effectively achieved by small electrically powered aircraft. As the charge is only emitted from a single point, further work is needed to establish the active area over which the charge is distributed. To achieve a greater effective release area, some alternative approaches could be considered. Fitting a set of emitters on a larger airframe provides one possibility; another, with greater volume coverage, would be through implementing an aircraft “swarm”, with multiple aircraft following the same flight pattern and simultaneously releasing charge across a range of altitudes.

Investigating geoengineering applications, whatever their ultimate societal value, is an increasingly urgent priority which is directly addressed by this technology. For this new application, electrically powered robotic aircraft provide adaptable delivery platforms without combustion products, and the charge released itself leaves no environmentally damaging residues.

Acknowledgements

This material is based on work supported by the National Center of Meteorology, Abu Dhabi, UAE under the UAE Research Program for Rain Enhancement Science (UAEREP). KAN acknowledges an Independent Research Fellowship funded by the Natural Environment Research Council, NERC (NE/L011514/1) and (NE/L011514/2). Stefan Chindea's involvement was supported by the NERC grant NE/N012070/1. Sam Hyams, James Male and Freddie Sherratt made valuable contributions to building and flying the aircraft. The meteorological sensor characterisation was undertaken by NERC SCENARIO summer students Heather Jones and Charlie Bell. Test flights in Finland were made during the 2019 Aerosol, Clouds and Trace Gases Research InfraStructure (ACTRIS) project in Pallas co-ordinated by the Finnish Meteorological Institute, a co-funded Institute of UAEREP. (ACTRIS-2 received funding from the European Union's Horizon 2020 research and innovation programme under grant agreement 654109; ACTRIS PPP is supported by the European Commission under the Horizon 2020 – Research and Innovation Framework Programme, H2020-INFRADEV-2016-2017, Grant Agreement: 739530). The University of Bristol provided access to Fenwood farm for flight tests.

Data availability

Data from the instrument tests are available from the corresponding author.

Appendix A - Meteorological sensor calibration

This section discusses the meteorological sensor package carried on the aircraft, and their calibration. The sensors consisted of a bead thermistor and an integrated relative humidity sensor (Honeywell HIH4000).

The RSPRO 10kΩ bead thermistor (type RS 151-237, 2.4mm diameter) was connected to a 10kΩ precision resistor to form a half-bridge, i.e. a potential divider from a regulated supply, giving a voltage output V_{THS}. The thermistor was calibrated against a standard Platinum Resistance Thermometer (PRT), T_{PRT} over a temperature range of -20 ˚C to 40 ˚C in an environmental chamber. Through this, the thermistor-bridge was found to have a first order linear response of

$$T_{PRT} = 20.397V_{THS} - 25.960 \quad \text{(A.1)},$$

for T_{PRT} in Celsius and V_{THS} in volts.

The HIH4000 humidity sensor was calibrated by placing it in an environmental chamber at 20 ^{o}C. The HIH4000's voltage output, V_{RH} was calibrated against a Michell dewpoint sensor in the chamber. The Relative Humidity (RH) within the chamber was increased from 30% to 100% in 5% steps. A first order response was found between the HIH4000's voltage output, V_{RH} and the RH measured from the dewpoint hygrometer RH_D of

$$RH_D = 30.547V_{RH} - 24.607 \quad \text{(A.2)},$$

for RH measured in % and V_{RH} in volts.

Appendix B – Cloud droplet sensor calibration

The calibration of the optical cloud sensor (OCS) is presented here. Its operation is described in Harrison and Nicoll (2014), but for this application it was extended to provide four channels. It consists of four high power light emitting diodes (LEDs) in an open path arrangement, with their backscattered light sensed by a photodiode mounted behind the LEDs. Two of the four LEDs are infra-red devices (peak emitting wavelength 850 nm), one cyan (505 nm) and one orange (590 nm), each of which is driven by a square wave at a unique frequency in the range between 1.1 kHz and 1.5 kHz. Any cloud droplets in the optical path from the LEDs will backscatter the modulated light, some of which is received by the photodiode. The photodiode signal is bandpass filtered to eliminate fluctuating daylight, so that only the modulated backscattered signal from the cloud droplets is retained. The independent square wave signals driving the LEDs are also used for phase-sensitive detection of the individual channels, to allow the photodiode signal to be decomposed into separate responses associated with each LED. Each of the four recovered signals is separately low pass filtered and amplified to yield a DC voltage output which is proportional to the backscatter, from which the size and concentration of water droplets are found by calibration.

The OCS was calibrated against a Light Optical Aerosol Counter (LOAC), described in Renard et al. (2015). The LOAC measures the concentrations of aerosol, dust and water droplets in the size range 0.1 μm to 50 μm range. It operates by pumping air through a laser chamber, with photodiodes mounted at 12^o and 60^o from the laser path to receive light scattered by droplets and particles. The number of forward scattered pulses received at each photodiode gives the concentration. By comparing the nature of the scattered light at each photodiode, information about the size and type of particle, e.g. carbon, mineral, ice or water can also be recovered. The LOAC returns concentrations in 17 size bins at 1 min resolution.

In a calibration experiment, two OCS devices were mounted alongside the LOAC above the surface on a 2.5 m mast, approximately 500 m from the River Thames in a large flat arable field on the University of Reading's Sonning farm (51.47^{o}N, 0.89^{o}W). This site experiences fog and river mists. The OCS devices were logged by an Arduino microcontroller operating in a similar manner to that used on the aircraft logging system. This arrangement was deployed in January 2019 for two months. During the 14th, 15th and 17th February 2019, fog events lasting several hours occurred at the site.

Figure B1 shows data from a fog event on the 15th February 2019. The fog formed at approximately 0700UTC and dissipated at 1200UTC. Only the infra-red channels of the OCS are considered here. The voltage outputs from the OCS' two infra-red channels are plotted in red and black, with LOAC droplet count (integrating across the several size bins that span the 10μm - 30μm range) in blue. The time series from the two instruments track well, showing the OCS response to fog droplets.

Figure B2 shows the raw ADC counts (IR_{ADC}), from the infra-red channel of one of the cloud sensors plotted against the integrated droplet count N_D from the LOAC. A least-squares fit to the data allows N_D to be calculated from the OCS' IR_{ADC}, as

$$N_D = (0.47 \pm 0.03) IR_{ADC} + (27.05 \pm 3.01) \tag{B.1}$$

Uncertainties in the fit are given by 95% confidence intervals, implying that the fitted line is robust despite the scatter. Mature fogs often have fairly consistent droplet sizes, hence the scatter evident may indicate changes in the droplet size distribution during the fog evolution.

The derived calibration was applied to both the balloon-borne and aircraft OCS, as described in the main text. To reduce the effects of instrumental drift, the drive signal to each LED was made steady (*i.e.* without square wave modulation) every 4 mins for 10 s, to effectively provide a zero for that channel without changing the balance of currents flowing in the overall device. This reference value was subsequently subtracted from the observed signal. As noise was also present on the OCS channels, the calibration was only applied when the mean backscattered signal from a 10 s moving window was greater than the mean and one standard deviation of the background noise from the whole flight.

References

Aplin, K.L., K.L. Smith, J.G. Firth, B.J. Kent, M.S. Alexander, J.P.W. Stark. Inexpensive optically isolated nanoammeter for use with micro-Newton electric propulsion technology. *J.Propulsion and Power* **24** (2008) 891-895

Banerjee S. and M. Levy. Exact closed-form solution for the electrostatic interaction of two equal-sized charged conducting spheres *J Physics Conf*, 646, 012016 doi:10.1088/1742-6596/646/1/012016 (2015)

Cheney, M. *Tesla: Man out of time* (Simon and Schuster, 1st touchstone edition) (2001)

Davis, M.H. Two charged spherical conductors in a uniform electric field: forces and field strength *Quart Journ Mech & Appl Math*, **17**, 4, 499-511 (1964)

Duft, D., T. Achtzehn, R. Müller, B.A. Huber, T. Leisner, Rayleigh jets from levitated microdroplets *Nature*, 421, 128 (2003)

Gaunt, L.F., J.F. Hughes, N.M. Harrison. Electrostatic deposition of charged insecticide sprays on electrically isolated insects *J. Electrostatics* **57**, 1, 35-47 (2003)

Gunn, R. Diffusion charging of atmospheric droplets by ions and the resulting combination coefficients. *J. Meteorol*, 11, 339–347 (1954)

Harrison, R.G. An antenna electrometer system for atmospheric electrical measurements *Rev Sci Instrum* **68**, 3, 1599-1603 (1997).

Harrison, R.G. A wide-range electrometer voltmeter for atmospheric measurements in thunderstorms and disturbed meteorological conditions *Rev Sci Instrum* **73**, 2, 482-483 (2002)

Harrison, R.G. and K.S. Carslaw, Ion-aerosol-cloud processes in the lower atmosphere *Rev Geophysics* **41** (3), 1012, 10.1029/2002RG000114 (2003)

Harrison, R.G., and K.A. Nicoll. Note: Active optical detection of cloud from a balloon platform. *Rev Sci Instrum*, **85**(6), 066104 (2014)

Harrison, R.G., K.A. Nicoll and A.G. Lomas, Programmable data acquisition system for research measurements from meteorological radiosondes. *Rev Sci Instrum*, 83(3) 036106 (2012)

Harrison, R.G., K.A. Nicoll, M.H.P. Ambaum. On the microphysical effects of observed cloud edge charging *Quart J Roy Meteorol Soc* 141, 2690-2699 (2015)

Harrison, R.G., G.J. Marlton, K.A. Nicoll, M.W. Airey, P.D. Williams. Note: A self-calibrating wide range electrometer for in-cloud measurements. *Rev Sci Instrum*, *88*(12), 126109 (2017)

Harrison, R.G., K.A. Nicoll, M.H.P. Ambaum, G.J. Marlton, K.L. Aplin, M. Lockwood. Precipitation modification by ionisation *Phys Rev Letters* **124** (19) 10.1103/PhysRevLett.124.198701 (2020)

Howard, L., *Seven Lectures on Meteorology,* Lecture 5. (1837, In: Second edition, Harvey and Dalton, 1843).

Ieta, A., M. Chirita. Electrohydrodynamic propeller for in-atmosphere propulsion; rotational device first flight *J Electrostatics* 100, 2019, 103352 (2019)

Inculet, I.I., G.S.P. Castle, D.R. Menzies, R. Frank, Deposition studies with a novel form of electrostatic crop sprayer, *J. Electrostatics* 10 65–72 (1981)

Kent, B.J., K.L. Aplin, L. Wang, S.E. Huq, R. Stevens, A. Malik, and D. Nicolini, A field effect spacecraft neutralizer for the LISA Pathfinder mission. *Classical and Quantum Gravity*, *22*(10), p.S483 (2005)

Lekner, J. Electrostatics of two charged conducting spheres. *Proc. R. Soc. London* A 468: 2829-2848, doi: 10.1098/rspa.2012.0133 (2012)

Nicoll, K.A. Note: A self-calibrating electrometer for atmospheric charge measurements from a balloon platform. *Rev Sci Instrum*, *84*(9), 096107 (2013)

Nicoll, K.A. and R.G. Harrison. Stratiform cloud electrification: comparison of theory with multiple in-cloud measurements. *Quart Jour Royal Meteorol Soc*, *142*(700), 2679-2691 (2016)

Phelps, C.T., and Vonnegut, B., Charging of droplets by impulse corona, *J Geophys Res*, 75(24), 4483-4490, https://doi.org/10.1029/JC075i024p04483 (1970)

Pruppacher, H.R., and J.D. Klett, *Microphysics of Cloud and Precipitation.* 2nd edition*,* Kluwer Academic Publishers (1998)

Rayleigh, Lord. The influence of electricity on colliding water drops. *Proc Roy Soc* **28**, 406-409 (1879)

Rayleigh, Lord. On the equilibrium of liquid conducting masses charged with electricity. *The London, Edinburgh, and Dublin Philosophical Magazine and Journal of Science* 14(87) 184-186 doi:10.1080/14786448208628425 (1882)

Renard, J.B., F. Dulac, G. Berthet, T. Lurton, D. Vignelle, F. Jégou,... & Akiki, R. LOAC: a small aerosol optical counter/sizer for ground-based and balloon measurements of the size distribution and nature of atmospheric particles–Part 2: First results from balloon and unmanned aerial vehicle flights. *Atmos Measure Tech Discus*, *8*(1), 1261-1299 (2015)

Russell, A. The problem of two electrified spheres *Proc Phys Soc Lond* **35** 10-29 (1922)

Takahashi, T. Measurement of electric charge of cloud droplets, drizzle, and raindrops. *Reviews of Geophysics and Space Physics*, *11*(4), 903-924. (1973)

Thomson, W. On the mutual attraction or repulsion between two electrified spherical conductors, pp. 86–97. (1853, In *Reprint of papers on electrostatics and magnetism*. London, UK. Macmillan, 1884)

Tripathi S.N. and R.G. Harrison. Scavenging of electrified radioactive aerosol *Atmos Environ* 35, 33, 5817-5821 (2001)

Vaisala RS41 datasheet. https://www.vaisala.com/sites/default/files/documents/RS41-SG-Datasheet-B211321EN.pdf (Visited 30/03/2020), (2018)

Vonnegut, B., C.B. Moore, G.E. Stout, D.W. Staggs, J.W. Bullock, W.E. Bradley, Artificial modification of atmospheric space charge *J Geophys Res* 67, 3, 1073-1083 (1962a)

Vonnegut, B., C.B. Moore, G.E. Stout, D.W. Staggs, J.W. Bullock, W.E. Bradley, Effect of atmospheric space charge on initial electrification of cumulus clouds *J Geophys Res* 67, 10, 3909-3922 (1962b)

Xu, H., Y. He, K.L. Strobel *et al.* Flight of an aeroplane with solid-state propulsion. *Nature* 563, 532–535 (2018). https://doi.org/10.1038/s41586-018-0707-9

Tables

Table 1. Summary of instrumented flights conducted.

Date	Local time	Flight duration (minutes)	Max altitude (m)	Location	In-cloud duration (minutes)
24/09/2019	11:30	15	1000	Pallas	0
24/09/2019	16:30	15	1450	Pallas	0
25/09/2019	14:15	16	1450	Pallas	1
25/09/2019	15:30	17	1450	Pallas	1
26/09/2019	12:10	22	1575	Pallas	5
27/09/2019	09:15	17	1950	Pallas	5
27/09/2019	10:45	21	2050	Pallas	1
28/09/2019	09:20	17	1150	Pallas	0
28/09/2019	12:10	15	1400	Pallas	1
28/09/2019	12:50	20	1315	Pallas	2
01/10/2019	09:25	18	815	Pallas	0
29/11/2019	13:45	22	100	Bristol	0
29/11/2019	14:55	17	100	Bristol	0

Figures and figure captions

Figure 1

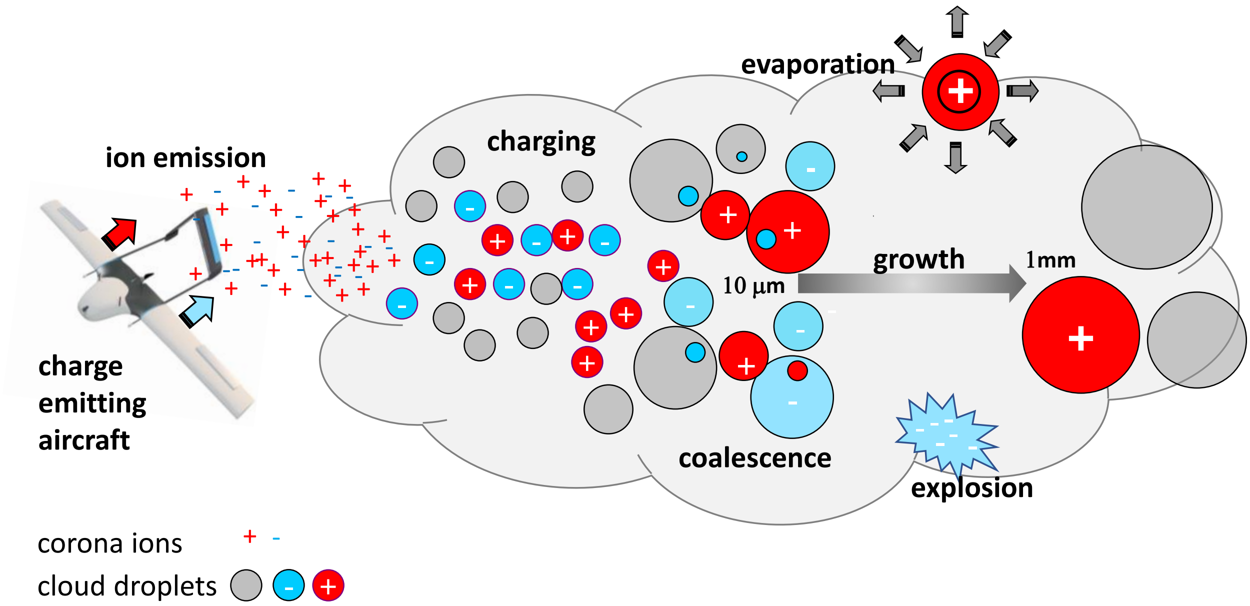

Figure 1. Conceptual picture of charge emission, droplet charging and droplet growth in a cloud (drawn to show droplet growth left to right). Corona ions released by an aircraft become entrained into the cloud, charging the water droplets present by attachment of the ions. Charging of the droplets modifies the droplet-droplet coalescence, influencing the growth rate to large drops which ultimately fall out of the cloud as rain. (Droplets lost by evaporation, or in the case of highly charged drops, charge-induced explosions which occur through electrical instability, are indicated at the cloud boundaries).

Figure 2

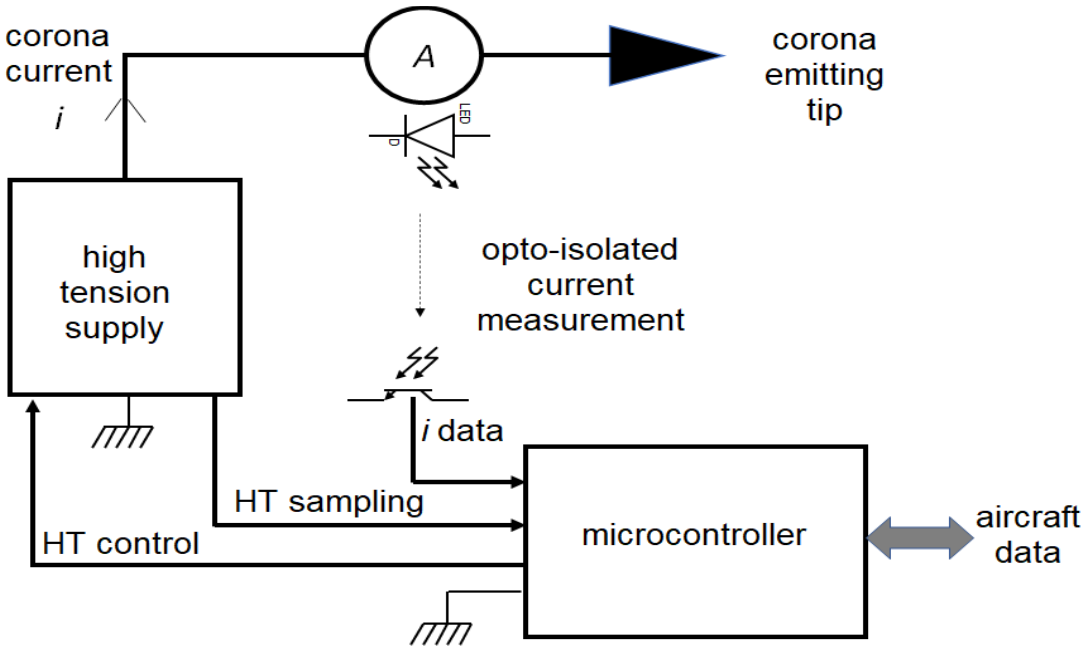

Figure 2. Corona emitter block circuit diagram. A miniature high voltage generator (EMCO A-series, A60P-5 for positive, A60N-5 for negative) is used to generate sufficient voltage to generate corona at the emitting tip. The HT voltage is set by the main microcontroller (AT-Tiny 84), using a 12-bit DAC (MCP4725) to control a MOSFET-based op-amp regulator circuit. The HT voltage is sampled by the same microcontroller using a 1000:1 resistive divider potential divider, at 10 bits resolution. The corona current flowing to the tip is sampled on the high voltage side (using an AD8293G160 instrumentation amplifier with gain of 160) and digitised at 10 bits resolution by a further microcontroller, with the values transmitted serial over an optically-isolated link (OPTEX OPI1264C) to the main microcontroller. Control of the emitters is achieved by data exchange with the aircraft systems, which also provide data telemetry to the surface.

Figure 3

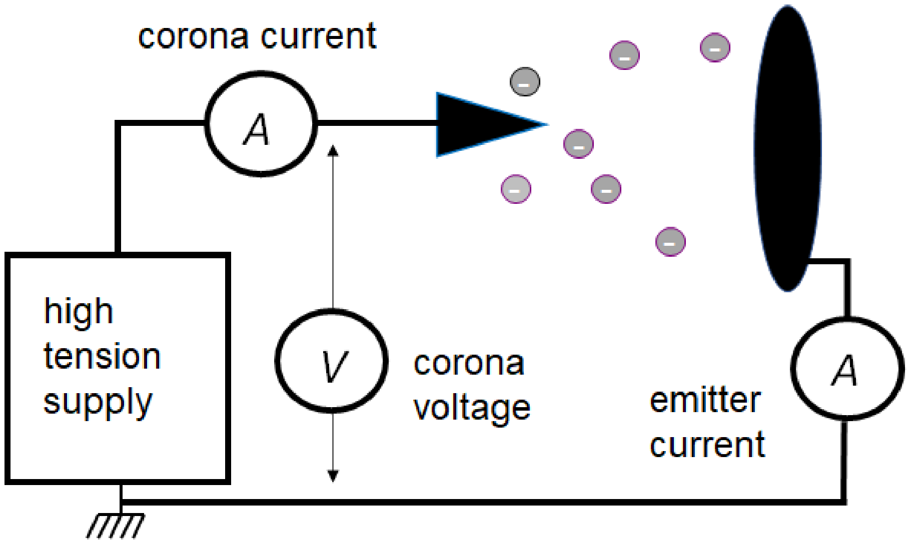

Figure 3. Conceptual diagram of the test system for a single charge emitter. A controlled high voltage is applied to an emitting tip (black arrow), and the corona current determined using the isolated measurement system of figure 2. The current emitted is also sampled at a nearby detection plate (shown by the black ellipse). For current balancing, a second opposite polarity emitter can be applied to the other side of the detection plate.

Figure 4

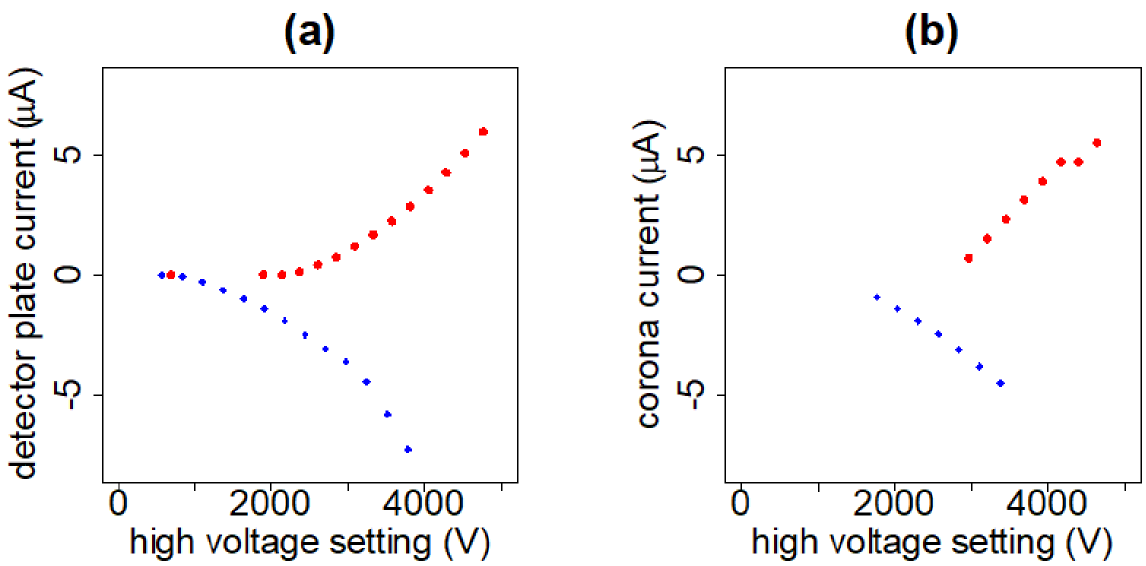

Figure 4. Tests on the corona emitters. (a) Ion current measured at the detector plate of figure 3 as the high voltage setting (HT voltage) on the corona tip was varied, in separate experiments. (b) Relationship between current measured by the on-board corona current measurement circuit and HT voltage. (In both cases, red points are for the positive emitter and blue for the negative emitter).

718 Figure 5

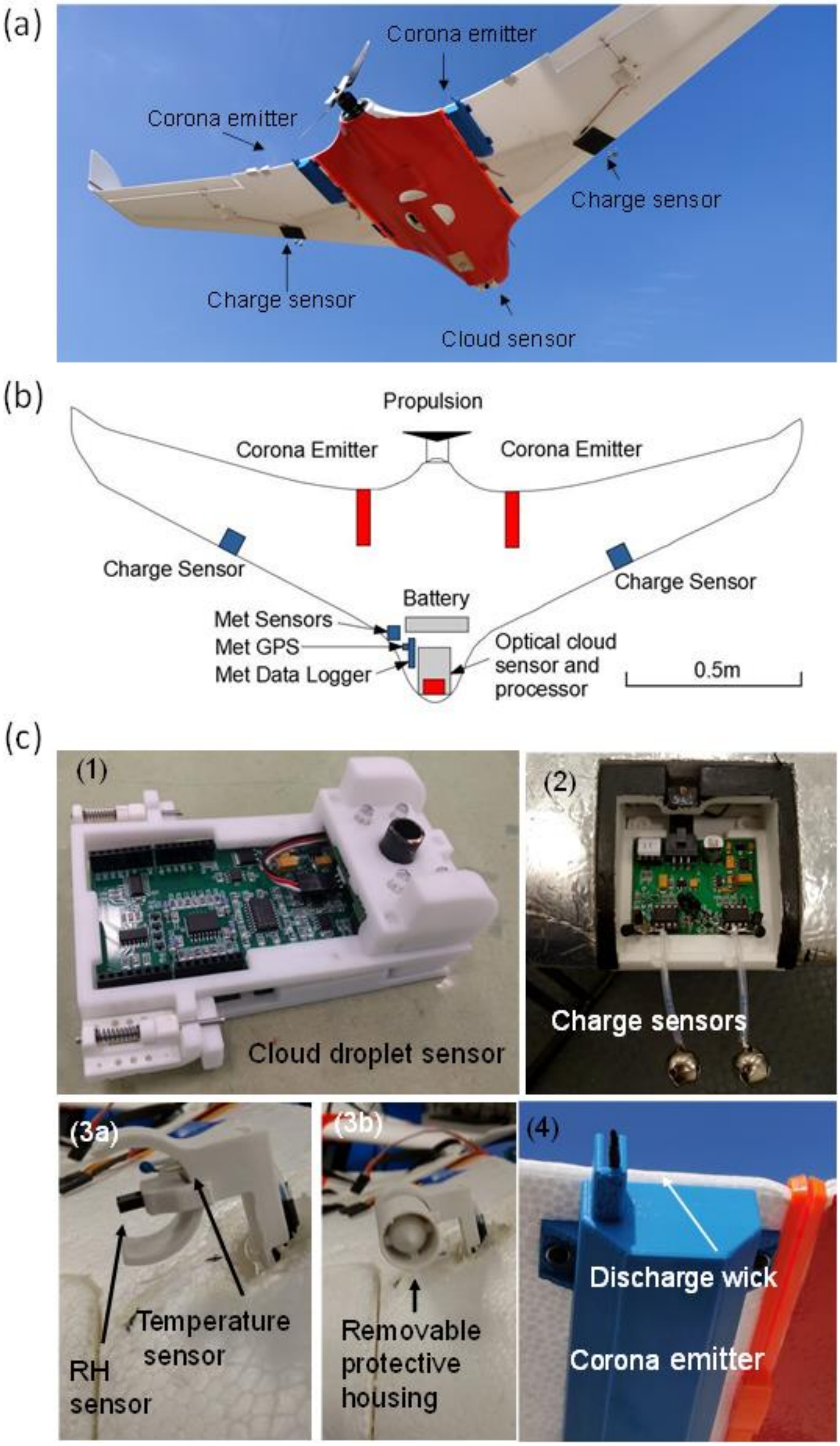

719

Figure 5. (a) Instrumented Skywalker X8 aircraft in flight, with instrumentation labelled. (b) Arrangement of sensors and systems on the X8 airframe (not to scale). (c) Detail of the individual science instruments: (1) optical cloud sensor, (2) charge sensors, (3a) thermodynamic (temperature and RH) sensor, (3b) removable protective housing for thermodynamic sensor, and (4) corona emitter electrode.

Figure 6

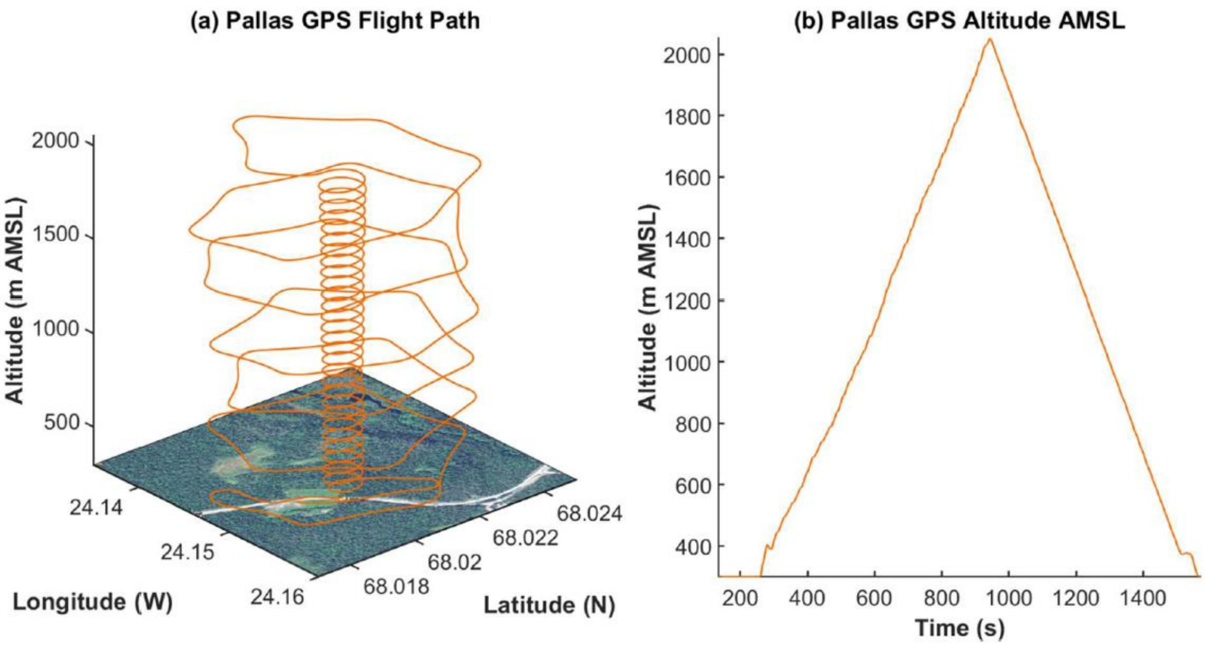

Figure 6. (a) Flight path and (b) altitude reached by the X8 during the longest endurance flight undertaken at Pallas at 1045LT on 27th September 2019.

Figure 7

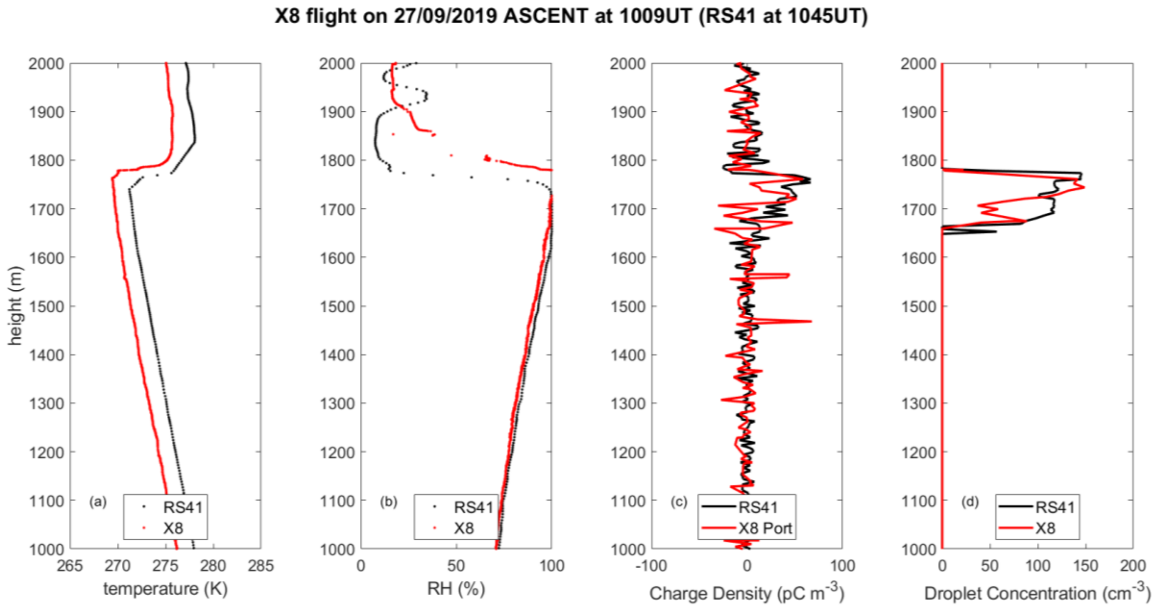

Figure 7. Comparison of radiosonde (RS41, released at 1045 UTC) and aircraft (X8, flown at 1009 UTC) profiles on the 27th September 2019. These are for (a) temperature, (b) relative humidity, (c) charge density, found from the portside charge sensor on the X8 and (d) droplet concentration, using a nose-mounted optical cloud sensor on the X8. (X8 data is in red and RS41 data in black).

Figure 8

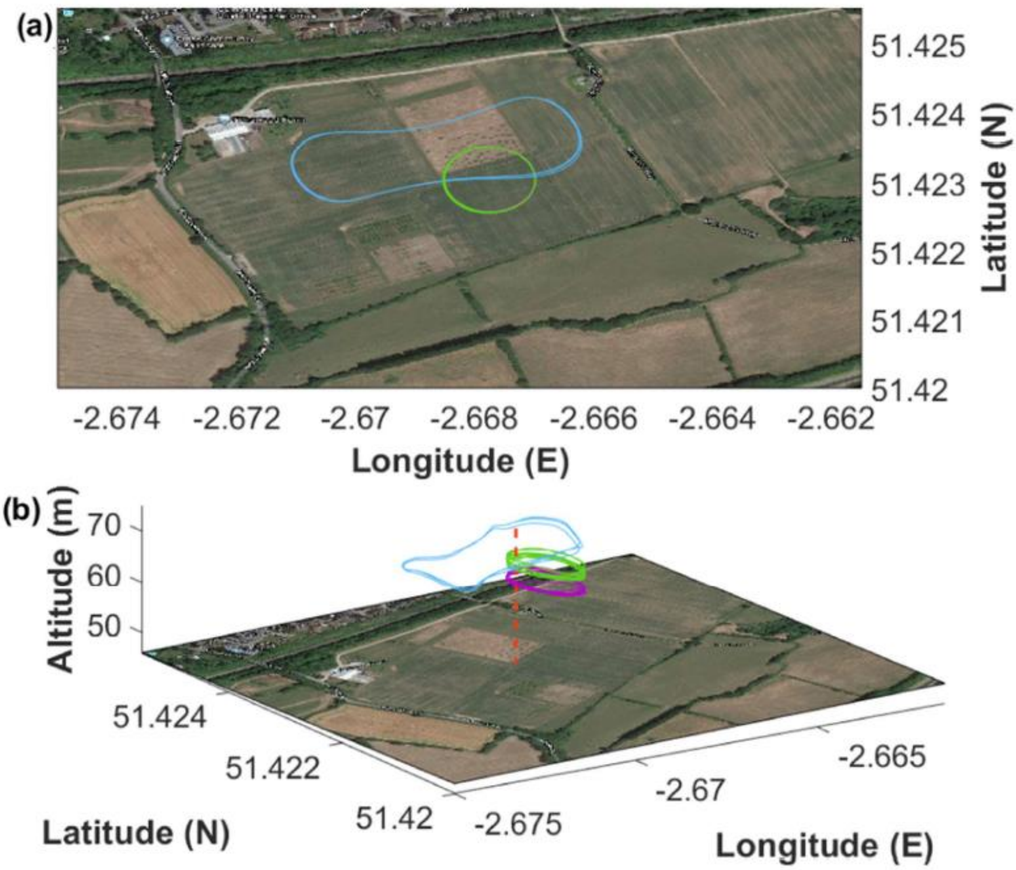

Figure 8. (a) Bird’s eye view of the flight path of the aircraft showing the square path (light blue) and circular loiter path (green and purple). (b) Three-dimensional view of the flight path with the square pattern at 20m altitude (light blue), 50m radius loiter at 20m altitude (green) and the 50m radius loiter at 15m altitude (purple), centred on the surface field mill location (dashed red vertical line).

Figure 9

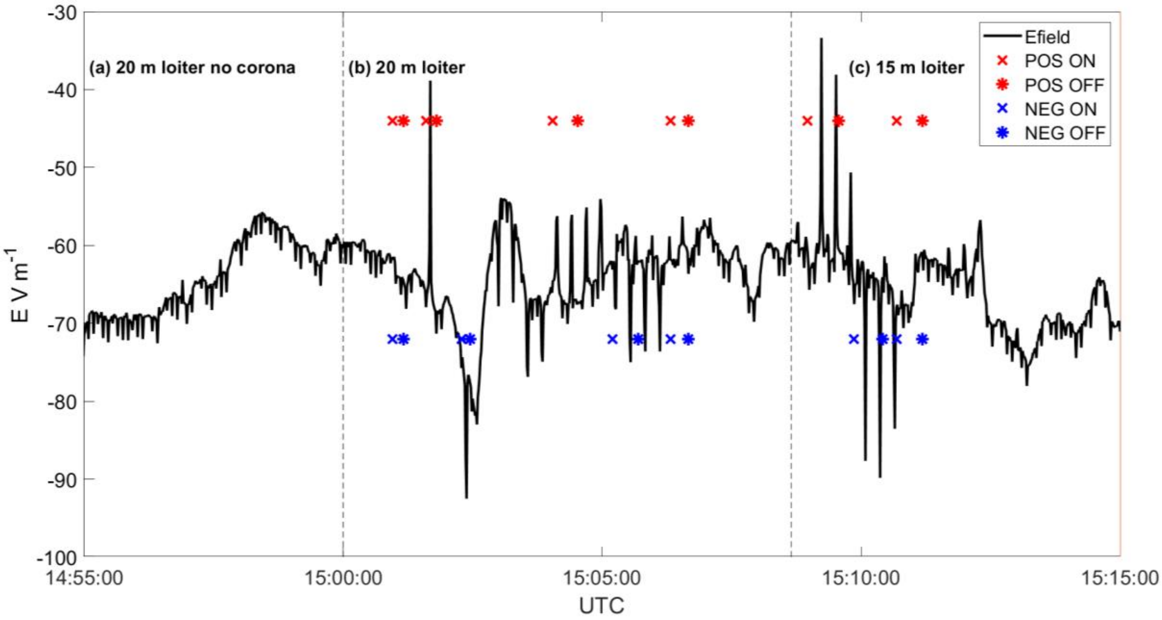

Figure 9. Time series of electric field (*E*) from the Chubb JCI131 electric field mill at Fenwood Farm on 29th November 2019, with the instrumented X8 aircraft flying overhead in different flight patterns. The flight patterns were (a) loiter but no corona emitters activated, (b) 20 m and (c) 15 m radius loiter with corona emitters cycled. Crosses and asterisks mark when the charge emission was switched on and off respectively, with blue and red used to indicate the positive and negative charge emitter respectively.

Figure 10

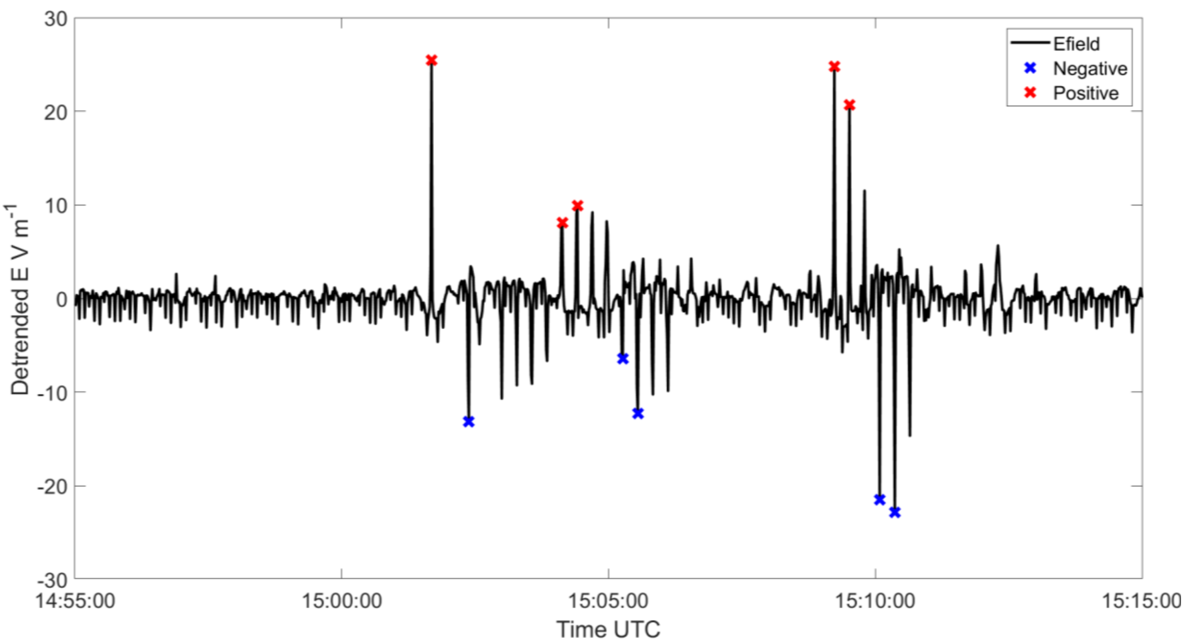

Figure 10: Detrended electric field (*E*) from the Chubb JCI131 electric field mill at Fenwood Farm on 29th November 2019, from figure 9. (Red and blue crosses identify electric field transients from which the charge released was calculated).

Figure B1

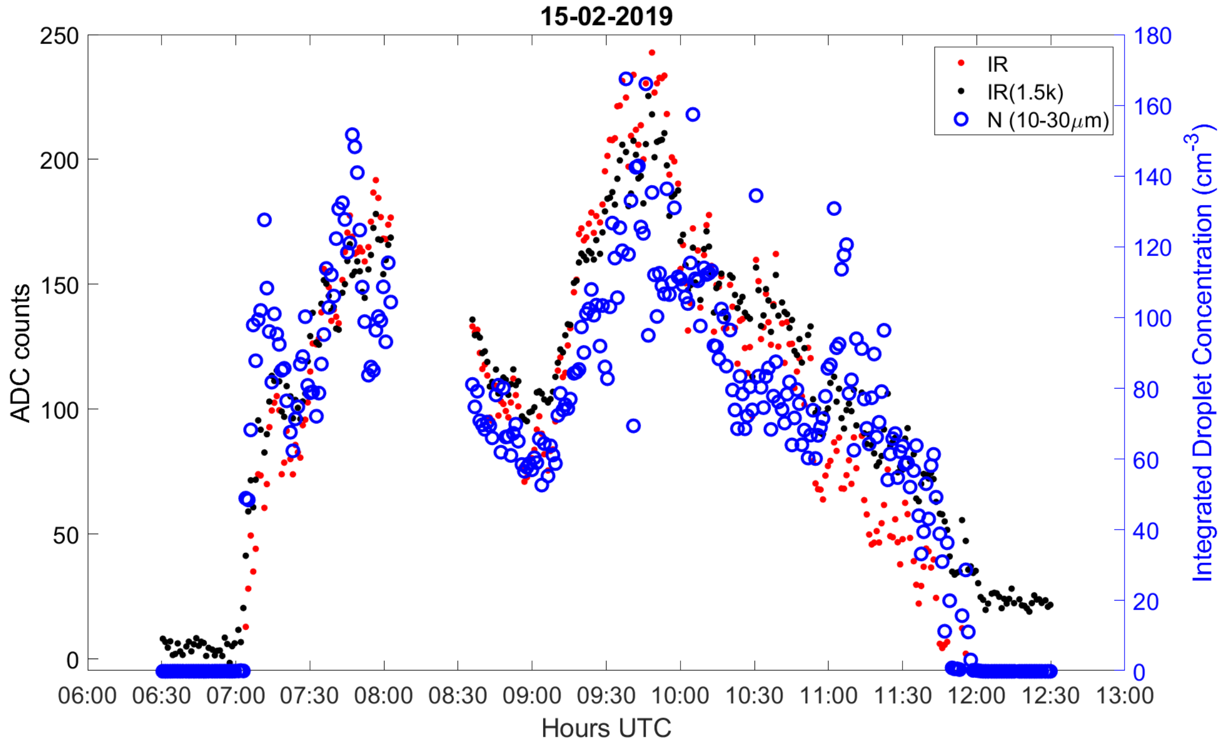

Figure B1. Comparison of OCS and LOAC devices. Time series showing the Analogue-to-Digital Converter (ADC) voltage counts from the two IR cloud sensor channels (black and red) and the integrated droplet count (blue) across the 10μm to 30μm diameter bins from the LOAC between 0600UTC and 1300UTC on 15th February 2019.

Figure B2

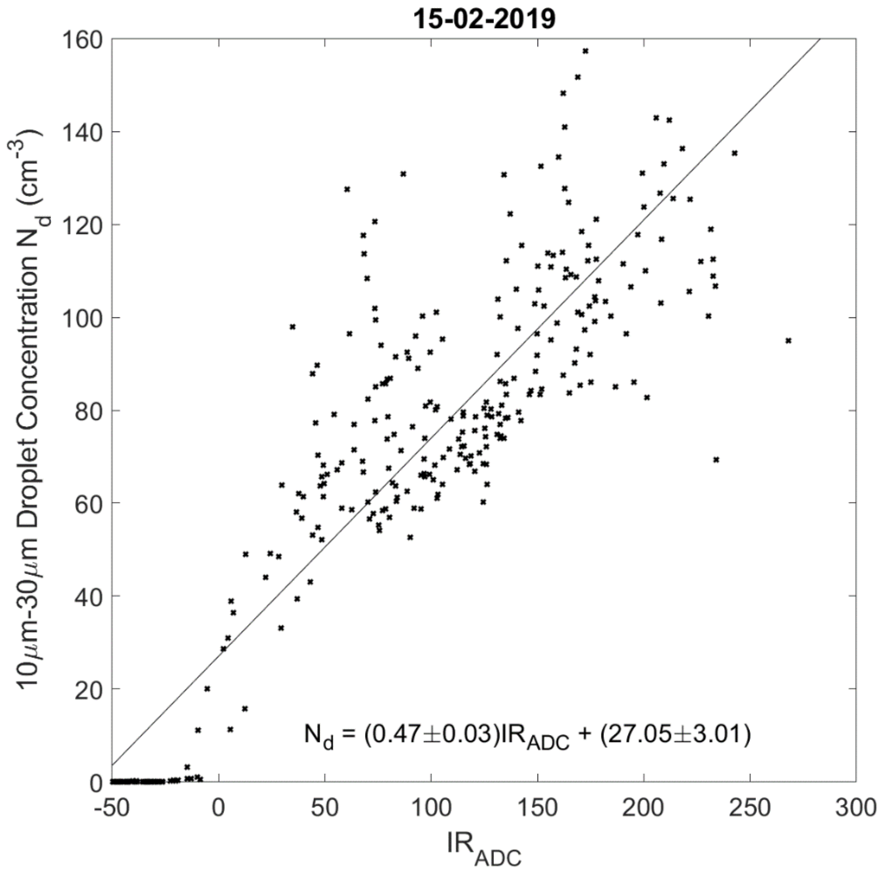

Figure B2. Comparison of OCS and LOAC devices. Infra-red channel ADC counts (IR_ADC) of the OCS plotted against the LOAC integrated droplet count (10-30μm size range) for all fog events during the 14th, 15th and 17th February 2019.